ACS NANO

Open Access

www.acsnano.org

ARTICLE

Emergent Thermal Strain-Induced Pseudomagnetic Fields and Shubnikov–de Haas Beating Patterns in Encapsulated Graphene in Extraordinary Magnetoresistance Geometry

Bowen Zhou,* Alina Mreńca-Kolasińska, Kenji Watanabe, and Takashi Taniguchi

Cite This: *ACS Nano* 2025, 19, 29276–29285

Read Online

ACCESS | Metrics & More | Article Recommendations | Supporting Information

ABSTRACT: **Strain has been theoretically predicted and experimentally demonstrated as a tool for modifying the properties of graphene and two-dimensional (2D) materials through the creation of a pseudomagnetic field (PMF). The practical introduction of a controllable PMF has so far presented a significant challenge. In this study, we present evidence for the presence of PMF induced by thermal strain in extraordinary magnetoresistance (EMR) devices based on monolayer graphene encapsulated in hexagonal boron nitride. Signal processing methods permit the differentiation of weak effects obscured within the signals. Investigations of the beating patterns in the Shubnikov–de Haas oscillations observed in electrical transport measurements complemented by finite element simulations and quantum transport calculations indicate the existence of a PMF of 0.1−0.2 T. The magnitude and pattern of strain and PMF in such geometry are flexible to control compared to other methods. The devices under investigation also exhibit an enhanced EMR effect, commensurability magnetoresistance effect, and weak localization and antilocalization due to spatial variation of strain in the device. The EMR geometry represents an intriguing and promising avenue for both fundamental physics research and applications including magnetic field sensors, straintronics and valleytronics, and 2D material and thin-film semiconductor industries.**

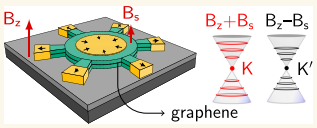

KEYWORDS: *graphene, strain, pseudomagnetic fields, Shubnikov–de Haas oscillations, extraordinary magnetoresistance, weak localization, weak antilocalization*

INTRODUCTION

Strain engineering has become popular in recent years for manipulating the valley degree of freedom in graphene, with the applications of valley filtering and splitting devices,[1] information encoding with polarized valleys,[2,3] and flat band generation.[4] The generation of an inhomogeneous magnetic field with sharp spatial variations represents a significant challenge for science; however, strain engineering offers a potential alternative solution for the creation of such a pseudomagnetic field (PMF). A controllable and easy-to-reach high pseudomagnetic field in graphene devices could help the study in quantum anomalous Hall effects and quantum valley Hall effects,[5,6] as well as previously inaccessible high magnetic field regimes.[7] The methods to induce strain in devices include using nanopillars or bumps,[3,7,8] sample bending,[2,9] and layer twisting.[5,6] However, strain and PMF are not easy to control through these methods. Other ways to induce a flexible PMF are desired.

Strain-induced PMF has been reported by local imaging methods,[6,10] but under-reported and therefore underrated by transport measurements of which the results can be strongly influenced as strain and PMF can modify materials' properties. Further study on strain and PMF is desired for applications in the 2D material industry and thin-film semiconductor industry.

Since its discovery in 2000, the extraordinary magnetoresistance (EMR) effect has been studied extensively at room temperature[11−15] primarily for the considerations of room-temperature applications in magnetic field sensors and hard disk drives; only a few studies have been performed at low temperatures.[16−19] However, by lowering the temperature, the carrier mobility in devices increases through reduction of electron−phonon scattering, and the EMR effect can be enhanced.[20]

Received: March 20, 2025
Revised: July 3, 2025
Accepted: July 7, 2025
Published: August 11, 2025

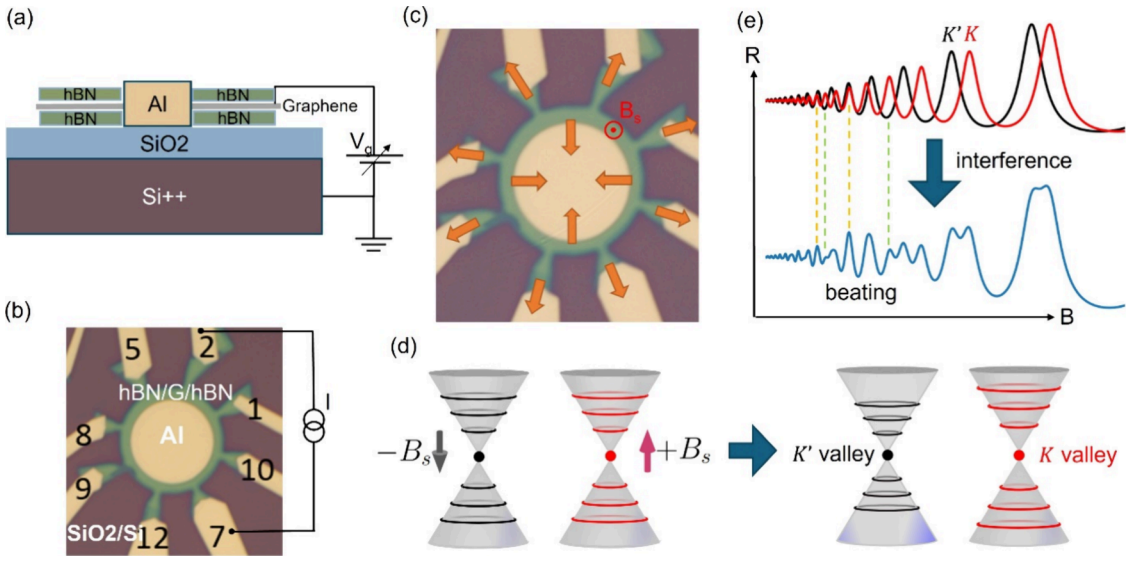

Figure 1. Strain-induced PMF in the EMR device. (a) Schematic side view of the EMR device. (b) Optical microscope image of device 1. (c) Schematic of strain distribution and PMF (B_s) in the device. (d) Schematic of LLs in K and K' valleys in the presence of PMF. (e) Schematic of Shubnikov–de Haas oscillations and beating pattern resulting from the interference of the LLs of K and K' valleys.

On the other hand, most physics studies on graphene devices use Hall geometry, and some use circular geometry as Corbino geometry in which the charge carriers primarily move along the radial axis. There are only a few experimental studies based on graphene in EMR geometry so far,[12,18,21,22] in which the charge carriers move in circular paths in the circular graphene channel[12,22] (Supplementary Figure 9) and could have resonance with the device geometry. Some peculiar effects that are associated with cyclotron orbits and device geometry could appear at low temperatures and await to be studied.

In this work, we demonstrate EMR geometry as an alternative way for strain engineering in graphene devices: by using thermal strain in the metal shunt that leads to stretching graphene, the nonuniform strain field and, consequently, the PMF with spatial variations result in the device. This is demonstrated by the beating patterns found in the Shubnikov–de Haas oscillations. We believe that the EMR geometry could pave the way to a controllable PMF and lead to developments in strain engineering and valleytronics. Furthermore, we also observe other phenomena including the commensurability magnetoresistance effect and weak localization and antilocalization effects as a consequence of the strain, suggesting EMR geometry as an interesting alternative to the Hall geometry for fundamental physics studies. Strain can reduce the intervalley scattering and restore the weak antilocalization (WAL) resulting from the chiral nature of carriers in graphene.[23] This work may further advance the transport measurement study on strain and PMF and make an impact on 2D material and thin-film semiconductor industries, as metals are the necessary components.

RESULTS

Emergent Strain-Induced Pseudomagnetic Field. Figure 1a,b shows the schematic side view and optical microscope image of EMR device 1 made by a hexagonal boron nitride (hBN)-graphene-hBN stack (details in Methods). For the background of the EMR effect and the characterization of the EMR devices from room to low temperatures, see Supplementary Notes A and B, respectively. Upon cooling to a low temperature, the central metal shunt and metal leads experience thermal contraction that stretches graphene and results in strain (Figure 1c). The nonuniform strain can lead to pseudomagnetic field (PMF) B_s in graphene,[24] which breaks the degeneracy of K and K' valleys. With applied magnetic field B perpendicular to the device, Landau levels (LLs) appear. The effective fields experienced by the charge carriers in K and K' valleys are $B - B_s$ and $B + B_s$, respectively (Figure 1d) that scale LLs differently in K and K' valleys according to the energy of the Nth LL $E_N^{\pm} \propto \sqrt{(B \pm B_s)|N|}$ (details in Methods).[6] The resulting two sets of Shubnikov–de Haas (SdH) oscillations have slightly different frequencies, and their interference could result in beating patterns (Figure 1e): constructive interference occurs and the amplitude increases when the two SdH oscillations are in-phase (yellow dashed line); the amplitude decreases when they are out-of-phase; destructive interference and a beating node appear when they are completely out-of-phase (green dashed line). Here, we present the experimental data and theoretical models to demonstrate these emergent phenomena in the EMR devices.

Beatings in Shubnikov–de Haas Oscillation. The device 1 exhibits both the EMR effect and the commensurability magnetoresistance effect[25,26] (Figure 2a) at 10 K from two-terminal measurements with the current flowing from terminal 2 to 7 (more discussion is in Section Commensurability Magnetoresistance). From around 1 to 9 T, SdH oscillation is exhibited in the resistance trace (Figure 2a) and reflects itself also in the two-terminal sensitivity dR/dB trace obtained by differentiation shown in Figure 2c, demonstrating the high quality of the device. For the background of magnetic field sensitivity, see Supplementary Note A. Beating patterns appear in SdH oscillations as a function of the perpendicular magnetic field. They are most prominent from 1 to 4 T at V_g = 20 V and from 2 to 4 T at V_g = 55 V. Beatings are the interference patterns between two waves of slightly different frequencies, showing a periodic variation in amplitudes. Constructive (destructive) interference of two waves results in a larger (smaller) amplitude. With a periodicity of $1/B$, the SdH oscillations can be plotted against $1/B$ and show four clear beating patterns (Figure 2d). Similarly, the beating patterns also appear in the two-terminal

https://doi.org/10.1021/acsnano.5c04844
ACS Nano 2025, 19, 29276–29285

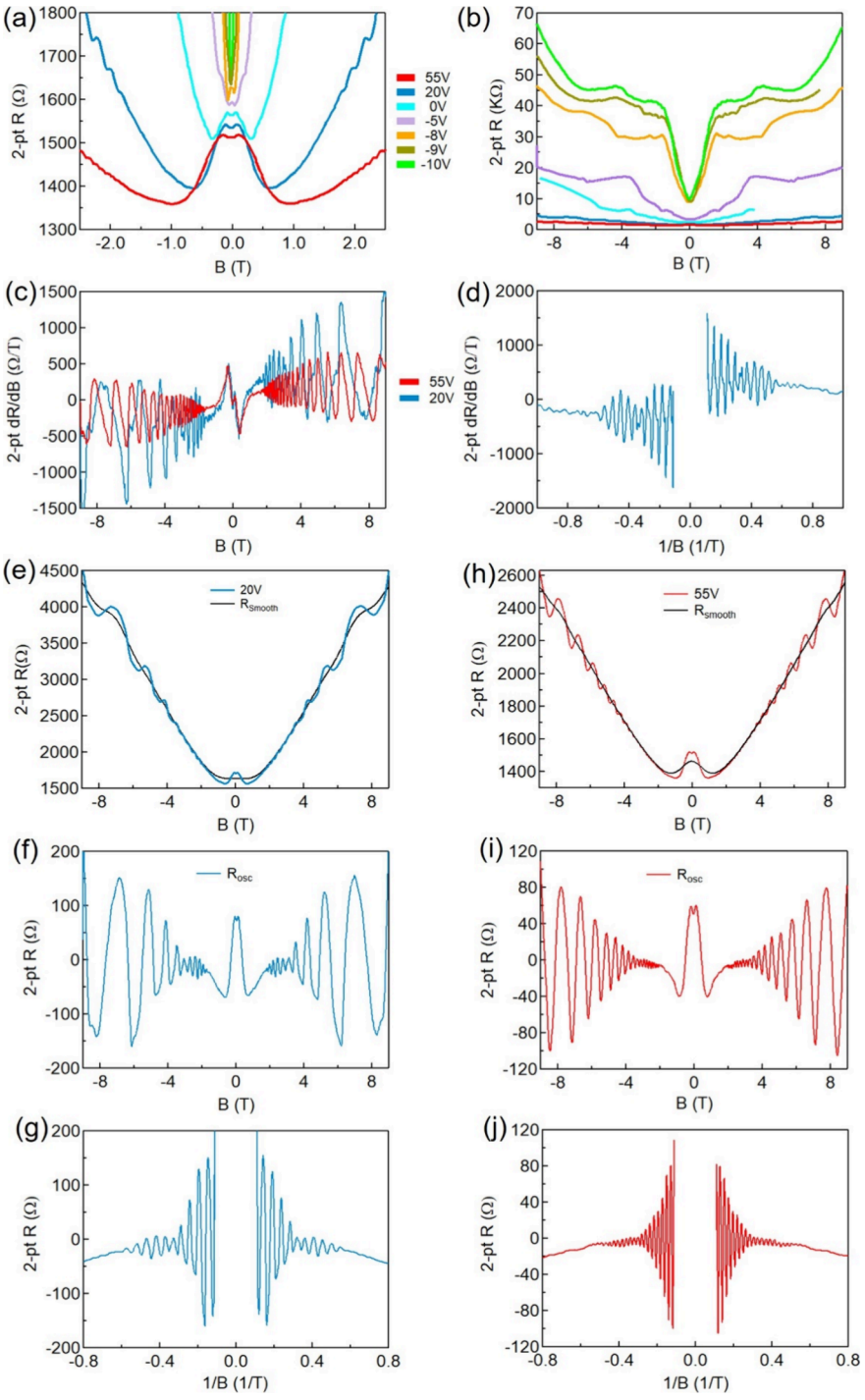

Figure 2. Commensurability magnetoresistance and beatings in Shubnikov−de Haas oscillation. (a) Two-terminal resistance of device 1 as a function of magnetic field B at 10 K at different gate voltages showing the commensurability magnetoresistance effect and SdH oscillations. Each curve was offset vertically for clarity. (b) Full range of two-terminal resistance traces shown in (a). Two-terminal sensitivities dR/dB as a function of (c) magnetic field B and (d) $1/B$ at gate voltages V_g = 55 and 20 V at 10 K calculated from (a) showing Shubnikov−de Haas oscillation and beating patterns. (e, h) Smoothed data R_{smooth} of two-terminal resistance as a function of magnetic field at 10 K at gate voltages V_g = 20 and 55 V. Oscillation part R_{osc} of two-terminal resistance as a function of (f, i) magnetic field B and (g, j) $1/B$ at 10 K at gate voltages V_g = 20 and 55 V.

sensitivity of device 2 at V_g = 0 V at 10 K (Supplementary Figure 1).

The original signals of resistance traces (Figure 2a) have large slopes due to the EMR effect that make the superposed beating patterns hard to identify. While the differentiation method presented above can help remove the slope from the signal, we also employ a different way for signal processing: Here, we first smooth the resistance data with binomial smoothing to remove the oscillations (Figure 2e,h) and subtract the smoothed data R_{smooth} from the original R to obtain the oscillation part R_{osc}, which indeed shows similar beating patterns (Figure 2f,i). R_{osc} as

https://doi.org/10.1021/acsnano.5c04844
ACS Nano 2025, 19, 29276−29285

a function of $1/B$ are shown in Figure 2g,j. Thus, we confirm the existence of the beating patterns in the resistance traces.

Origins of Beatings and Strain. The beating patterns have been reported to come from Rashba spin−orbit coupling (SOC) that mixes the spin-up and spin-down states of neighboring Landau levels into two unequally spaced energy branches.[27,28] However, graphene has a negligible intrinsic SOC[29] and requires the proximity effect of high-atomic-number semiconductors[30−32] to show a high SOC. Alternatively, the strain-induced pseudomagnetic field (PMF) can lead to the valley-polarized Landau levels and interference and consequently the beating patterns[6] observed in the graphene EMR devices.

The strain in our devices is not expected to come from the alignment or twist angle between layers in the hBN-monolayer graphene-hBN stack,[6,33] so it should have a different source. Metals in the central shunt and the leads of the EMR devices can experience two thermal contraction processes: one from the cooldown process from high to ambient temperature after deposition on a substrate following electron beam evaporation and the other from the cooldown process from ambient temperature to measurement temperature at 10 K in a cryogenic system. The total strain in Al is estimated as $\varepsilon_{tot} = -5.686 \times 10^{-3}$ (more details in Methods). The resultant thermal strain in the metal could be passed to graphene via an edge contact. The large central metal shunt pulls graphene inward, and the eight metal leads stretch graphene outward; complex patterns of strain and stress could eventually result in graphene (Figures 1c and 3b, d, and e). This method may provide a possible route for a nonuniform strain profile that is proposed to produce PMF and a pseudomagnetic quantum Hall effect in ref 24.

Theoretical Models for the Pseudomagnetic Field. In this section, we provide several methods to estimate PMF in the device, with the first one using the beating node position[6] in the measurement at V_g = 20 V (Figure 2c,f). The destructive interference (first beating node) of the valley-polarized LLs in device 1 appears at the LL index $N_b^1 = 7$ corresponding to the applied magnetic field B = 2.8 T (details in Methods). The PMF can be calculated as $B_s = \frac{B}{4N_b^1} = 100$ mT. We also use COMSOL simulation to study the stress distribution in the device with the prescribed displacement 2.5587×10^{-8} m on all metal−graphene interfaces including the boundaries of the central shunt and six leads (Figure 3b, simulation details in Methods). Figure 3d,e shows the site displacements plotted in x and y directions separately to show the displacement directions. Indeed, graphene is deformed toward the center and pulled outward by the leads. We export the data of site displacements and estimate the PMF to be $|B_s| \lesssim 0.25$ T based on ref 8 with PMF distribution shown in Figure 3c (details in Methods). To make a more precise estimation, we built a tight-binding model (model details in the Methods) to obtain the plot of R_{xx} in response to magnetic field B and charge density n (Figure 3f). The R_{xx} map shows the splitting of Landau levels, which suggests that the PMF lifts the valley degeneracy. By fitting two sets of Landau levels to the spectrum, each shifted by $\pm B_s$, we estimate the PMF at 0.2 T. Note that the transport data give an overall value averaged over some area of the device.

We also calculate the density of states (DoS) and fit the experimental data to estimate the PMF (details in the Methods). To this end, the two-terminal experimental data obtained in device 1 at V_g = 20 V is used (see Figure 2c). Figure 3g shows the DoS calculated as a function of B and n, with the beating nodes visible as modulation of DoS, and marked by the red dashed line

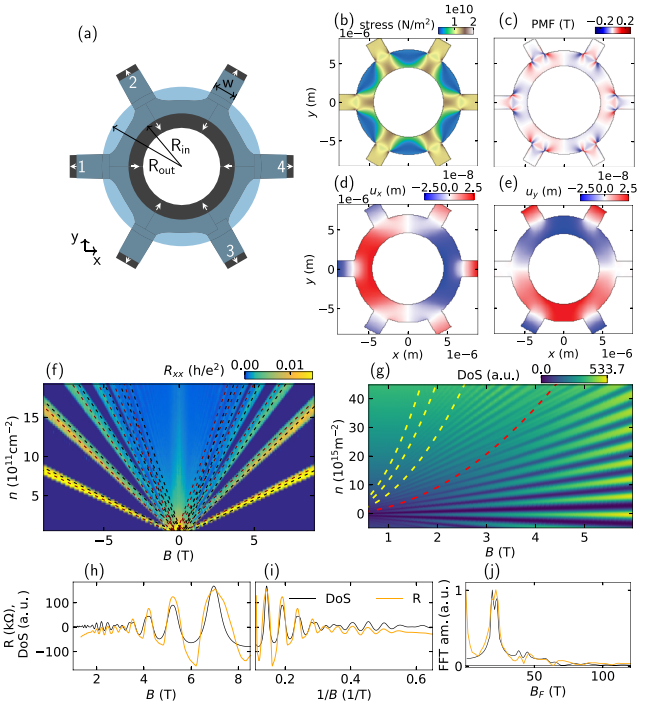

Figure 3. Simulations of stress, PMF, Landau fan, and density of states. (a) Schematic of the system used for the quantum transport calculations with white numbers labeling the leads. Blue semi-transparent is the unstrained system, and the dark gray is under strain with the displacement multiplied by 10 to show the deformation more clearly. White arrows indicate the direction of deformation. (b) Stress distribution in device 1 simulated by COMSOL Multiphysics. The device geometry is simplified to facilitate the tight-binding calculation. (c) Calculated PMF distribution in the device based on-site displacement data exported from COMSOL simulation. (d) x component and (e) y component of the displacement field from COMSOL simulation. (f) R_{xx} in response to B and n calculated using the tight-binding model. The dashed lines are LLs calculated for the K (red) and K' (black) valleys with B_s = 0.2 T. (g) Density of states calculated with B_s = 0.105 T and Γ = 3.5 meV. The red dashed line indicates the position of the first beating node N_b^1, and yellow dashed lines indicate higher beating nodes N_b^2 to N_b^4. The experimental resistance R_{osc} (yellow) and the calculated density of states (DoS) (black) with PMF = 0.105 T in response to (h) magnetic field B and (i) $1/B$. (j) Normalized fast Fourier transform of the experimental resistance R_{osc} (yellow) and the DoS (black) with a PMF of 0.105 T.

(first beating node) and yellow dashed lines (higher beating nodes). Figure 3h,i shows experimental data R_{osc} (yellow) and the calculated DoS (black) at the corresponding charge carrier density with PMF B_s = 0.105 T in response to magnetic field B and $1/B$, respectively. The fast Fourier transform (FFT) of the $R_{osc}(1/B)$ data in Figure 3j shows the splitting of the first peak, originating from the $\pm B_s$ shift of the spectra in each valley. R_{osc} and DoS as well as their corresponding FFTs all show good agreement (for other exemplary values of B_s = 0.095−0.115 T, see Supplementary Figure 2). Discussion about the red trace at V_g = 55 V is in Supplementary Note C. Supplementary Figure 3a−c shows the R_{osc} and DoS and FFTs of the two-terminal experimental data at V_g = 0 V (light blue) in Figure 2a,b with the estimation of B_s = 0.215 T. We also use the four-terminal experimental data of device 1 with current flowing from probe 2 to 7 and voltage measured across probes 1 and 10 at V_g = 0 V and estimate the PMF to be ∼0.106 T (Supplementary Figure 3d−

https://doi.org/10.1021/acsnano.5c04844
ACS Nano 2025, 19, 29276−29285

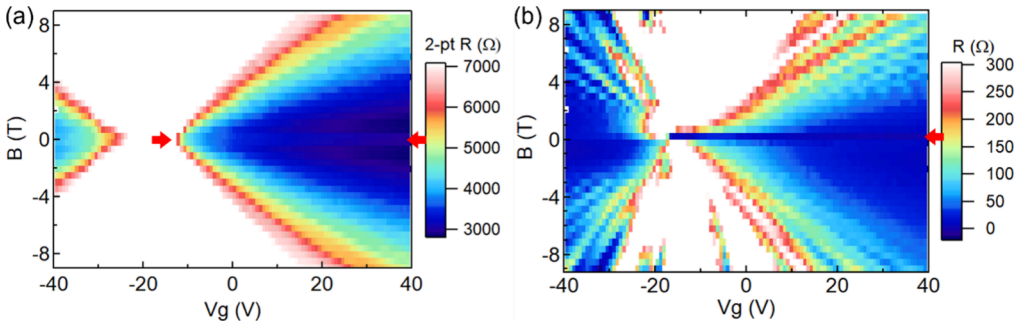

Figure 4. Weak localization and weak antilocalization. 2D plots of (a) two-terminal resistance and (b) four-terminal resistance of device 2 in response to B and V_g at 10 K. The color represents the magnitude of resistance. The red arrows indicate the presence of WL and WAL, respectively.

f). These methods lead to the conclusion that the PMF in our device is 0.105−0.215 T with spatial variations.

Weak Localization and Weak Antilocalization. In Figures 3f and 5a, we can spot a dip (dark blue) in resistance around B = 0 T, indicating the occurrence of weak antilocalization (WAL). It is reported that the strain could lead to a bandgap opening and occurrence of WAL.[9,23,24] The Berry phase π and chirality of the carriers in graphene would ideally lead to WAL; however, the presence of short-range scatterers breaks the chirality and induces intervalley scattering, resulting in weak localization (WL). Ref 23 reported WL suppression as a result of the reduction of the intervalley scattering due to strain. Here, strain can even restore the WAL.

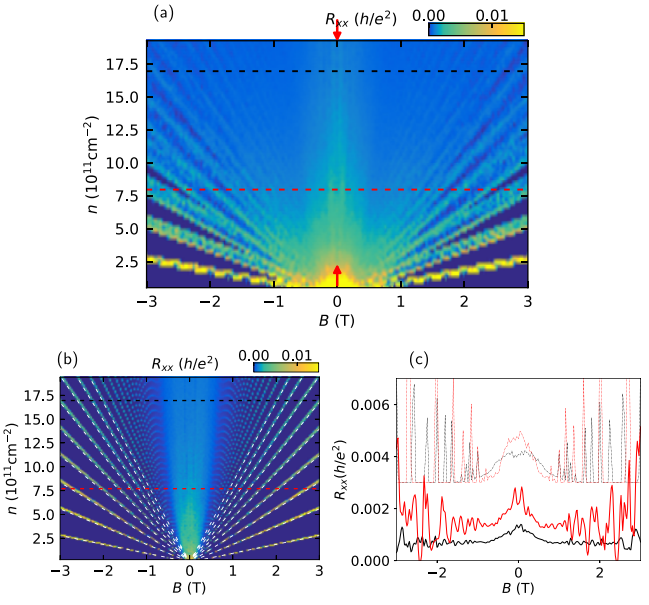

Figure 5. R_{xx} in response to B and n calculated by a tight-binding model. (a) Low magnetic field zoomed-in image of Figure 3f in the main text, with the presence of strain in the device. Around $B \approx 0$, a minimum of R_{xx} is visible, between the red arrows, indicating the presence of WAL. (b) R_{xx} as a function of the magnetic field and density without the presence of strain in the device. The calculation was done in the same system as described in the main text, with a random disorder amplitude of 0.02 eV, averaged over 10 disorder realizations. The white dashed lines mark a few of the lowest analytical Landau levels. (c) Line cuts of R_{xx} as marked in (a, b). The solid lines show R_{xx} in response to B at $n = 8.04 \times 10^{11}$ cm^{-2} (red) and 17.42×10^{11} cm^{-2} (black), with strain, extracted from (a), showing the coexistence of WAL and WL in agreement with the experimental data in Supplementary Figure 4a. The dash-dotted lines show R_{xx} without strain, extracted from (b). The dash-dotted lines are vertically offset by 0.003° for clarity.

Fabricated from the same encapsulated graphene stack, device 2 exhibits both WL and WAL of carriers (Supplementary Note D). The 2D plots of the two-terminal resistance and four-terminal resistance in response to B and V_g at 10 K are taken from the two-terminal measurement with the current flowing from terminal 12 to 7 and the four-terminal measurement with the additional voltage terminals 4 and 10 (inset of Supplementary Figure 8f), respectively. A light blue stripe (higher resistance) around 0 T with a consistent width (marked by a red arrow) immersed in the dark blue region (lower resistance) of the electron-doping region in Figure 4a suggests the presence of the WL effect. A narrower dark blue stripe (lower resistance) around 0 T with a consistent width immersed in the light blue region (higher resistance) of the electron-doping region in Figure 4b suggests the presence of WAL, in qualitative agreement with the simulations (Figures 3f and 5a). Similar consistencies in WAL and WL have also been reported in graphene on WS_2[34] and graphene-on-hBN devices.[35] However, both the WL and the WAL effects in device 2 are not as obvious in the hole-doping region because the Fermi level pinning (FLP) and the resultant band realignment and pn junction near the metal−graphene interface lead to a higher resistance in this region.[21,36]

WL and WAL can exist in different regions of our EMR devices due to spatial variation of strain (Figure 3b, d, and e), which may suppress WL and restore WAL.[23] Supplementary Figure 4 also shows the appearance of WL and WAL in two-terminal measurement and four-terminal measurement, respectively, of device 1 at 10 K. WL and WAL seem to coexist and compete with each other at −50 V in Supplementary Figure 4a, demonstrated as a dip in a bump in four-terminal resistance, in agreement with the simulated R_{xx} at, for example, $n = 8.04 \times 10^{11}$ cm^{-2} (red solid line) and 17.42×10^{11} cm^{-2} (black solid line) in Figure 5c, suggesting the effects of strain for suppressing and restoring localization effects. Two-terminal measurements reflect the holistic properties of the device, while four-terminal measurements primarily reflect the local properties of graphene in a region close to the two voltage probes. This is demonstrated in Supplementary Figure 4 as the voltage trace looks qualitatively similar to the resistance trace from four-terminal measurement and both show coexistence of WAL and WL, while the current trace and the resistance trace from two-terminal measurement shows only WL. Similarly, transition between and coexistence of WAL and WL have also been found in the graphene Hall bar.[37]

https://doi.org/10.1021/acsnano.5c04844
ACS Nano 2025, 19, 29276−29285

Ref 35 reported WL in graphene-on-hBN devices at $T = 250$ mK as the phase coherence time is larger than the intervalley scattering time and appearance of WAL when T approaches 10 K due to shorter phase coherence time. WAL is also reported in the suspended graphene Corbino disk,[38] which has a circular geometry and edge contact with the central metal like EMR geometry; it is possible that EMR and Corbino geometries could share some similarities in the strain pattern.

For comparison, the plot of R_{xx} in response to magnetic field B and charge density n in unstrained graphene from a quantum transport calculation is presented in Figure 5b. The resulting longitudinal resistance map does not show splitting of the Landau levels: see the white dashed lines marking a few of the lowest analytical Landau levels. Additionally, in this simulation, the WAL is absent or very weak, which, however, is observed in a strained sample. This difference is presented in Figure 5c, where the solid lines and the dash-dotted lines show line cuts at densities marked in Figure 5a,b. A very faint resistance minimum close to $B = 0$ might be spotted in Figure 5b, but it is not seen consistently at all densities. It could result from the competition of the π Berry phase (which can in principle cause WAL in pristine graphene) and the intervalley scattering due to disorder (which breaks WAL).

Commensurability Magnetoresistance. The commensurable magnetoresistance effect can appear in a ballistic transport bulk system where the charge carriers undergo diffusive scatterings with the boundary. Figure 2a shows that the anomalous magnetoresistance peaks appear in device 1 at 10 K below $B = 0.5$ T owing to the magnetic commensurability effect between the cyclotron radius R_c and device size. We take the resistance trace at $V_g = 55$ V for example: as B increases from zero, R increases with B and exhibits a maximum at $B_{max} = \pm 0.12$ T, and then, R decreases with B and exhibits a minimum at $B_{min} = \pm 0.95$ T. For higher B, the Shubnikov–de Haas oscillation (SdH) is superposed on the EMR effect as R oscillates as a function of B. This anomalous magnetoresistance has a strong dependence on the gate voltage: the interval between the two minimum resistance points (valleys) in each resistance trace decreases from 1.9 T at 55 V to negligible at −9 V close to CNP, and the amplitude between the peak and the valley decreases from 159 Ω at 55 V to negligible at and below −9 V. The two-terminal resistance in the full magnetic field range at 10 K is shown in Figure 2b.

According to ref 25, the value of B_{max} scales with the ratio of the cyclotron radius R_c to the channel width W as $\alpha = W/R_c$. The graphene channel in EMR device 1 has a width of $W = 2.12$ μm. We calculate α based on the equation

$$\alpha = \frac{eWB_{max}}{\hbar\sqrt{\pi n}}$$

Here, we find that the average α is 1.078 in our device, almost in the range of expected 0.9 ± 0.1 for a ballistic graphene channel.[25] This suggests that some charge carriers could bounce between the outer edge of graphene and the interface between graphene and the central metal shunt at a low field and experience the circular graphene channel itself as separated from the central metal shunt (see current distributions in Supplementary Figure 9 (300 K)).

DISCUSSION

We are not aware of any report on pseudomagnetic fields resulting from thermal strain in evaporated metal in Hall geometry, possibly because the Hall bars generally have large open areas far from the metal leads. However, with a significantly small Hall bar, WAL is reported in the sample with a central channel of around 1 μm width made by monolayer graphene without hBN encapsulation,[39] possibly also resulting from the strain in the metal leads. We note that strain levels up to 0.12% have been reported to be induced by contacts in semi-encapsulated graphene/hBN Hall bars.[33] The strain pattern reported therein is contributed by expansion of graphene and contraction of gold leads when cooling as well as the difference between the thermal expansion coefficients of Au (positive) and graphene (negative). A higher strain is reported in unencapsulated graphene in contact with the Ni film than Ti and Au films.[40]

Different from the methods of twist angles between layers[5,6,33] and sample bending,[2,9] PMF induced by thermal strain in metal in EMR geometry is easy and flexible to change. The magnitude of strain and PMF can be changed by varying the measurement temperature to induce a different thermal deformation in metal, using metals with different thermal expansion coefficients or residual stress, and varying the metal thickness.[40] The pattern of strain and PMF in the device can also be varied by changing the geometry of the device, such as the number and widths of the probes in EMR devices, the outer boundaries of the device, the boundary between the shunt and graphene, *etc.* The material of the central shunt can also be a semiconductor or insulator. The advantage of using the device with a central insulating shunt is that the beating pattern in the resistance trace can be immediately identified without signal processing to deal with the slope of the resistance trace shown in Figure 2a as the current runs only through the graphene channel, and no EMR effect is involved. Graphene in the device can also be replaced by other 2D materials because the strain is primarily from the central shunt. We expect that this understudied EMR geometry can advance the fields of straintronics and valleytronics. Note that we do not need to retain the EMR geometry as the key idea is using geometry variations to control the patterns and magnitudes of stress and PMF in order to control K and K' valleys. Similar geometries such as Corbino and others could be explored in such a purpose. Corbino geometry can be regarded as a deformed EMR geometry with the metal probes shorted together at the outer boundary. Some theoretical works have proposed to utilize strain in Corbino geometry for valley manipulation, polarization, and filtering to carry information, analogous to spintronics.[41,42] Therefore, our finding can open the door to future practical realization by employing thermal strain in these geometries.

CONCLUSIONS

We have studied the low-temperature effects in encapsulated graphene devices in EMR geometry and found a new way, i.e., using thermal strain in the metal to induce a pseudomagnetic field, which is suggested by the presence of beating patterns in the SdH oscillations. Two methods are used for signal processing to identify the beatings, by differentiation and smoothing. Multiple methods are also used to estimate the magnitude of the pseudomagnetic field to be 0.1–0.2 T: using the LL index of the beating node, finite element simulations, quantum transport simulations, and density of states and Fourier transform. Additionally, we found many interesting geometry and quantum effects including the magnetic commensurability effect, weak localization, and weak antilocalization, which can be suppressed and restored due to spatial variation of strain in the

https://doi.org/10.1021/acsnano.5c04844
ACS Nano 2025, 19, 29276–29285

device. The appearance of these effects suggests EMR geometry as an interesting alternative to the Hall geometry for fundamental and applied physics studies. This work may further advance the transport measurement study on strain and PMF and make an impact on 2D material and thin-film semiconductor industries.

METHODS

Experimental Methods. The devices were manufactured from mechanically exfoliated monolayer graphene encapsulated in 30 nm-thick hBN flakes using a dry-transfer technique.[43] The hBN-graphene-hBN stack was placed on highly p-doped Si substrates with a 300 nm-thick SiO_2 top layer. The device geometry was defined by electron beam lithography (EBL) followed by reactive ion etching (RIE), resulting in disk-shaped devices of outer radius r_0 with concentric circular holes of inner radius r_i. Electrical contacts and a central metal shunt were then defined by EBL and electron beam evaporation of a 4/80 nm Ti/Al electrode layer. The schematic side view of the EMR device is shown in Figure 1a. Figure 1b and the inset of Supplementary Figure 8f show the optical images of device 1 with the inner radius $r_i = 4.5\ \mu$m and the outer radius $r_o = 6.6\ \mu$m and device 2 with the inner radius $r_i = 3.3\ \mu$m and the outer radius $r_o = 5.9\ \mu$m, respectively. Electronic transport measurements were carried out using a lock-in technique with a 200 μV bias at a frequency of 13 Hz in a variable-temperature physical property measurement system (PPMS) equipped with a 9 T magnet. The graphene carrier density n was controlled by a gate voltage V_g applied to the Si substrate. The rate of change in carrier density with gate voltage, $n = 6.42 \times 10^{10}\ V_g\ V^{-1}\ cm^{-2}$, was estimated by considering a 300 nm SiO_2 layer and a 30 nm bottom hBN layer, with relative dielectric constants 3.9 and 3.29, respectively. Measurements were performed at 300, 10, and 4 K.

Estimation of the Landau Level with Index *N*. For a rough estimation of the Landau level index, we can use the relation $E = \hbar v_F \sqrt{\pi n}$ and the Nth LL energy $E_N = \mathrm{sgn}(N)\sqrt{2e(B)\hbar v_F^2 |N|}$, where $N = 0, \pm1, \pm2$, and so on. Assuming that $N > 0$, the estimated B is $B = \frac{\hbar \pi n}{2eN}$. At $n = 19.6 \times 10^{15}\ m^{-2}$, it gives $B = 20.23$ T for the first LL and $B = 2.89$ T for the seventh LL, which is the position of the beating node in the blue trace in Figure 2c.

Estimation of Thermal Strain and PMF in Graphene. The metal evaporates at a temperature higher than its melting point in the electron beam evaporator and contracts during the cooldown process after deposition on a substrate. The melting point of Al is 660 °C, and the source−substrate distance in the electron beam evaporator is 69.85 cm. The temperature of Al atoms decreases during travel in the chamber due to radiation and scattering with residual molecules. The glass temperature (GT) of electron beam resists 495 and 950 PMMA is in the range of 95−106 °C, above which PMMA becomes soft and may not function. The temperature of Al atoms landing on the substrate (T_a) should be below GT of PMMA. Assuming that $T_a = 80$ °C, the temperature change $\Delta T = T_f - T_a = -60$°C, where $T_f = 20$ °C is the ambient temperature that Al cools to. The strain in Al can be estimated with linear thermal expansion:

$$\varepsilon_t = \frac{\Delta L}{L} = \alpha_L \Delta T = -1.386 \times 10^{-3}$$

where the linear thermal expansion coefficient (LTEC) $\alpha_L = 23.1 \times 10^{-6}\ K^{-1}$ at 20 °C, which is significantly larger than the LTEC of monolayer graphene $-3.2 \times 10^{-6}\ K^{-1}$ at room temperature.[44,45] We neglect the strain of graphene resulting from its own cooling in this calculation. The cooling from ambient temperature to 10 K results in extra strain in Al, $\varepsilon_c = -4.3 \times 10^{-3}$, based on NIST 6061-T6 aluminum (UNS A96061) and references.[46,47] The total strain in Al is $\varepsilon_{tot} = \varepsilon_t + \varepsilon_c = -5.686 \times 10^{-3}$. The stress in Al is $\sigma_{Al} = \varepsilon_{tot} E_{Al} = -420.764$ MPa, where $E_{Al} = 74$ GPa is the average Young's modulus of Al at low temperatures. The stresses in graphene and metal near the boundary should be the same, so the strain in graphene can be estimated as $\varepsilon_G = \frac{-\sigma_{Al}}{E_G} = 0.4007 \times 10^{-3}$. We may adopt the bent-ribbon model[6] in a small region of graphene, which reported a pseudomagnetic field of 6 mT in a sample with a corresponding in-plane bending strain of 5×10^{-5}, and estimate the PMF in graphene to be $B_s^{total} = 48.08$ mT. This is a very rough estimation due to approximations, and a more precise estimation is given in the Results Section Theoretical Models for the Pseudomagnetic Field.

COMSOL Model. We used COMSOL Multiphysics 6.1 for finite element simulations. To facilitate the quantum transport calculations, a symmetric design of geometry was used as shown in Figure 3a−e. The EMR device had an outer radius of $r_o = 6.6\ \mu$m and an inner radius of $r_i = 4.5\ \mu$m. The width of the probe was 2 μm. The material of the central shunt was Al with a density of 2700 kg/m^3, a Young's modulus of 70 GPa, and a Poisson's ratio of 0.33. The parameters of graphene were set as a density of 2267 kg/m^3, a Young's modulus of 1050 GPa, and a Poisson's ratio of 0.19.

In our 2D model, the Solid Mechanics module was used with a thickness of 0.335 nm. The total strain in Al was $\varepsilon_{tot} = -5.686 \times 10^{-3}$, as described in the main text. To obtain the site displacement, we used the approximation of a rectangle elongation in the normal directions for simplicity in this calculation although the shunt had a circular shape, and the prescribed displacement of each side of the metal shunt was calculated as

$$\Delta L = \frac{\varepsilon_{tot} L_{Al}}{2} = 2.5587 \times 10^{-8}\ \mathrm{m}$$

where $L_{Al} = 2r_i$ and $r_i = 4.5\ \mu$m is the radius of the metal shunt. The outer boundary of the device was set as free, excluding all of the metal−graphene interfaces.

Density of States Calculation. For an additional analysis of the measurement data, we calculated the density of states (DoS) for an idealized model of graphene with a uniform pseudomagnetic field $B_s = (0, 0, B_s)$ and in the presence of an external magnetic field $B = (0, 0, B)$. In this case, the energy of Nth Landau level (LL) is

$$E_N^{\pm} = \mathrm{sgn}(N)\sqrt{2e(B \pm B_s)\hbar v_F^2 |N|},\ N = 0, \pm1, \pm2, \ldots$$

where the $\pm B_s$ stands for the pseudomagnetic field in the K (K') valley. Then, DoS was calculated as a sum of contributions from the K and K' valleys

$$D(\varepsilon) = \frac{2e(B + B_s)}{h} \sum_N \delta(\varepsilon - E_N^+) + \frac{2e(B - B_s)}{h} \sum_N \delta(\varepsilon - E_N^-)$$

To account for the broadening of the LLs due to the presence of disorder, phonons, or impurities, we used the approximation of Dirac delta $\delta(\varepsilon)$ by the Lorentzian function with width Γ. In the limit of vanishing Γ, it recovers the Dirac delta:

$$\lim_{\Gamma \to 0} \frac{1}{\pi} \frac{\Gamma}{\Gamma^2 + \varepsilon^2} = \delta(\varepsilon)$$

Additionally, to convert the energy to density n for the presentation of $D(n)$, we used the formula for the carrier density at the zero temperature limit

$$n(\varepsilon) = \int_0^{\varepsilon} D(\varepsilon')\mathrm{d}\varepsilon'$$

which for the Lorentzian approximation can be calculated exactly

https://doi.org/10.1021/acsnano.5c04844
ACS Nano 2025, 19, 29276−29285

$$n(\varepsilon) = \frac{1}{\pi}\frac{2e(B + B_s)}{h}\sum_N [\arctan((\varepsilon' - E_N^+)/\Gamma)]_0^\varepsilon + \frac{1}{\pi}\frac{2e(B - B_s)}{h}\sum_N [\arctan((\varepsilon' - E_N^-)/\Gamma)]_0^\varepsilon$$

$$n(\varepsilon) = \frac{2e(B + B_s)}{h\pi}\sum_N [\arctan((\varepsilon - E_N^+)/\Gamma) - \arctan(E_N^+/\Gamma)] + \frac{2e(B - B_s)}{h\pi}\sum_N [\arctan((\varepsilon - E_N^-)/\Gamma) - \arctan(E_N^-/\Gamma)]$$

The DoS map calculated for B_s = 105 mT and broadening 3.5 meV is shown in Figure 3g, with Landau levels clearly visible. Moreover, several beating nodes can be seen in the map. The first beating node occurs at Landau level index $N_b^1 = B/4B_s$ according to ref 6. Then, using the energy of Nth LL $E_N = \mathrm{sgn}(N)\sqrt{2eB\hbar v_F^2|N|}$ neglecting the pseudomagnetic field and $E_N = \hbar v_F\sqrt{\pi n}$, we get the estimate of the beating node position in the n vs B plot $n = eB^2/hB_s$. The first beating node is plotted over the DoS map with a red dashed line. The higher beating nodes are marked with yellow dashed lines.

The experimental data were processed for comparison with the DoS, as shown in Figure 3h−j. First, the data were smoothed with the binomial smoothing. The oscillation part R_{osc} was obtained by removing the smooth background; then, $R_{osc}(1/B)$ was interpolated to get equally spaced $1/B$ data, and the result was Fourier transformed. The resulting FFT spectrum as well as the R_{osc} data can be compared to DoS, which is processed in the same way, and their values were downscaled by 2 and shifted by −120 in the y axis to match the experimental data.

Figure 3j shows the result together with the DoS calculated at density $n = 19.6 \times 10^{15}$ m^{-2}, with the experimental data corresponding to $V = 20$ V found to match well according to the position of the first peak of FFT of $R_{osc}(1/B)$, although the exact position of the charge neutrality point is not well-defined.

Quantum Transport Calculations. For the transport calculations, we use the tight-binding Hamiltonian

$$-\sum_{\langle i,j\rangle} t_{ij}c_i^\dagger c_j + \sum_i V(\boldsymbol{r}_i)c_i^\dagger c_i$$

where $c_i^\dagger(c_i)$ is the creation (annihilation) operator of electrons on site i at position $r_i = (x_i, y_i)$. The first sum runs over the nearest neighbors with the hopping parameter t_{ij}, and the second sum describes the on-site potential energy. To enable calculations for realistic sized devices, we used the scalable tight-binding model,[48] where the lattice constant a_0 = 0.25 nm and hopping parameter t_0 = 3 eV were scaled to $a = a_0 s_f$ and $t_{ij} = t_0/s_f$, with the scaling factor s_f = 8. To account for the presence of an external magnetic field perpendicular to the graphene plane $\boldsymbol{B} = (0, 0, B)$, the Peierls substitution $t_{ij} \to t_{ij}\exp(i\phi)$ was used, where $\phi = \frac{e}{\hbar}\int_{r_i}^{r_j} A\mathrm{d}r$. We used the vector potential $\boldsymbol{A}$ in the Landau gauge $\boldsymbol{A} = (-yB, 0, 0)$ and in the leads used the gauge transformation such that $\boldsymbol{A}$ satisfies the translational invariance of the respective lead.[49,50] In strained graphene, the site positions $\boldsymbol{r}_i$ are modified from the ones in unstrained graphene $\boldsymbol{r}_i^0 = (x_i, y_i)$ according to the displacement field (u_x, u_y) obtained from COMSOL simulation $\boldsymbol{r}_i = (x_i^0 + u_x(x_i^0, y_i^0), y_i^0 + u_y(x_i^0, y_i^0))$. The effect of strain was included in the scalable tight-binding Hamiltonian through the modulation of the hopping parameter $t_{ij} \to t_{ij}\exp(-\beta(d_{ij}/a_{cc}s_f - 1))$,[51] where d_{ij} is the distance between site i and j in the strained system, β = 3.37 is the decay coefficient, and a_{cc} is the bond length in the unstrained graphene. We included the s_f in the hopping modulation, but in the scaled tight-binding model, an additional modification of the displacement field was needed by replacing $(u_x, u_y) \to (s_f u_x, s_f u_y)$ to obtain the same pseudomagnetic field as in the nonscaled graphene lattice.[51] For the scattering problem, we used the wavefunction matching[52] within the Landauer−Büttiker formalism. In a multiprobe system, the conductance from lead i to lead j was calculated as $G_{ji} = \frac{2e}{h^2}T_{ji}$, where the transmission probability is summed over propagating modes $T_{ij} = \sum_q T_{ij}^q$. For the four-terminal resistance calculation in a multiterminal system, we assumed that two of the leads serve as voltage probes and two others as current probes. Then, the resistance $R_{ij,kl}$ with the current flowing between probes k and l, and the voltage taken between probes i and j, was obtained by solving the scattering problem for all the pairs of leads in the system.[49,53,54]

The model system for transport calculation was a ring-like graphene sheet with six rectangular contacts stretching out radially along the direction defined by the angles 0, ±60, ±120, and 180 deg. We did not include the metal shunt in the model for simplicity and since the COMSOL simulations showed that the current mostly propagates within graphene in a magnetic field (see Supplementary Figure 9). Two of the contacts were chosen as voltage probes, and two others as current probes. The x axis was taken along the zigzag direction of the graphene lattice. The outer (inner) radius of the ring is $R_{out} \approx 668$ nm ($R_{in} \approx 452$ nm), and the probe width $w \approx 198$ nm (Figure 3a). Limited by the computation power, the system used for quantum transport was 10 times smaller than the COMSOL model used for the calculation of displacement; therefore, the obtained displacement had to be additionally downscaled by a factor of 10 to obtain the same pseudomagnetic field. The schematic of the system is shown in Figure 3a. The nondeformed system is shown in blue semitransparent, and the system under strain is shown in dark gray (with the displacement multiplied by 10 for clarity). The colormaps in Figure 3d,e show the displacement components u_x and u_y, obtained from the COMSOL simulation. From the displacement, it is evident that graphene is pulled into the center by the circular metal shunt and outward by the metal contacts, as shown by small white arrows in Figure 3a.

Resistance $R_{xx} = R_{12,34}$ was calculated as a function of magnetic field and back gate voltage (see lead labeling in Figure 3a), assuming zero temperature and carriers incident at zero energy. The carrier density was calculated as $n = C_g V_g/e$, with $C_g/e = 0.642 \times 10^{15}$ m^{-2} V^{-1}, from which one can get the on-site energy as $V = -\mathrm{sgn}(n)\hbar v_F\sqrt{\pi|n|}$ to be input into the tight-binding Hamiltonian. Additionally, a disorder was modeled as random noise added to the on-site energy $\sum_i U_i c_i^\dagger c_i$ within $r < R_{out}$, where $U_i \in (-0.02, 0.02)$ eV is a random number following a uniform distribution. The resistance was averaged over 10 different disorder configurations. The results are presented in Figure 3f. The energy of the Landau levels shown by dashed lines requires correction by multiplying by 0.98 to fit the position of resistance maxima.[48]

Pseudomagnetic Field Calculation. We can obtain the pseudomagnetic field B_s from the calculated displacement profile.[8]

The relation between the pseudo vector potential $\boldsymbol{A}_s$ and the strain tensor ε elements is $\boldsymbol{A}_s = \frac{\hbar\beta}{2ea_{cc}}\begin{pmatrix}\varepsilon_{xx} - \varepsilon_{yy} \\ -2\varepsilon_{xy}\end{pmatrix}$ where the elements of the tensor are $\varepsilon_{ij} = \frac{1}{2}(\partial_j u_i + \partial_i u_j + (\partial_i u_z)(\partial_j u_z))$, $i, j = x, y$.

Since we only consider the in-plane displacement, the strain tensor elements reduce to

$$\varepsilon_{ij} = \frac{1}{2}(\partial_j u_i + \partial_i u_j),\ i, j = x, y$$

From this, one can obtain the pseudomagnetic field as

$$\boldsymbol{B}_s = \nabla \times \boldsymbol{A}_s = (0,\ 0,\ \partial_x A_{s,y} - \partial_x A_{s,x}) = (0,\ 0,\ B_s)$$

Possible Alternative Origin of Beatings: Small Density Variation. Suppose the splitting of the first FFT peak in Figure 3j is due to the different charge densities in two regions of graphene in the device (e.g., regions with different intrinsic doping), we can estimate these densities corresponding to the two FFT maxima. From the periodicity of SdH oscillations, the FFT peak should be at $n = \frac{4eB_F}{h}$. The two FFT maxima are at frequencies B_F = 18.85 and 22 T, corresponding to densities $n \approx 18.23 \times 10^{15}$ and 21.28×10^{15} m^{-2}, respectively. These densities differ by 3×10^{15} m^{-2}. The DoS calculated for two sets of LLs with a rigid shift in density by this value is shown in Supplementary Figure 5, in which the pattern looks qualitatively different from the result considering beatings due to a small PMF (Figure 3g). The positions of the beating nodes in Supplementary Figure 5 almost do not change with the charge densities and are also

https://doi.org/10.1021/acsnano.5c04844
ACS Nano 2025, 19, 29276−29285

different from the measured ones (i.e., beating nodes at V_g = 20 V at about 2.8 T and at V_g = 55 V at about 3.4 T). Therefore, we exclude the possibility that the density variation in the sample is the only origin of the beatings, but we cannot rule out the possibility of its presence in our devices along with the existence of PMF.

ASSOCIATED CONTENT

Data Availability Statement

The data sets generated and analyzed during the current study are available from the corresponding author on reasonable request.

Supporting Information

The Supporting Information is available free of charge at https://pubs.acs.org/doi/10.1021/acsnano.5c04844.

Additional experimental data including beating patterns in two-terminal transport data, weak localization and weak antilocalization, and temperature and gate dependence measurements; additional simulation data including density of states calculation with various pseudomagnetic fields, density of states calculated with different intrinsic doping, and COMSOL simulation of current distribution; background of the EMR effect and sensitivity; Supplementary Figures 1−9, Supplementary Notes A−F, and SI references (PDF)

AUTHOR INFORMATION

Corresponding Author

Bowen Zhou − *Department of Physics, Technical University of Denmark, Kgs. Lyngby 2800, Denmark;* orcid.org/0000-0002-5373-8186; Email: nerozh@outlook.com

Authors

Alina Mreńca-Kolasińska − *Faculty of Physics and Applied Computer Science, AGH University, Krakow 30-059, Poland;* orcid.org/0000-0003-0083-5182

Kenji Watanabe − *Research Center for Electronic and Optical Materials, National Institute for Materials Science, Tsukuba 305-0044, Japan;* orcid.org/0000-0003-3701-8119

Takashi Taniguchi − *Research Center for Materials Nanoarchitectonics, National Institute for Materials Science, Tsukuba 305-0044, Japan;* orcid.org/0000-0002-1467-3105

Complete contact information is available at: https://pubs.acs.org/10.1021/acsnano.5c04844

Author Contributions

B.Z. designed the experiment, fabricated the devices, performed the measurements and analyzed the data, performed the finite element simulation, and wrote the manuscript. A.M.-K. performed transport calculations and wrote the manuscript. K.W. and T.T. provided the hBN samples.

Notes

The authors declare no competing financial interest.

ACKNOWLEDGMENTS

B.Z. acknowledges discussions with Erik Henriksen, Peter Bøggild, Antti-Pekka Jauho, Victor Rosendal, Simone Latini, Pengru Huang, Ying Liu, Jorge Estrada-Álvarez, Timothy John Booth, and Mads Brandbyge and acknowledges funding from the Novo Nordisk Foundation, grant no. NNF21OC0066526 (BioMag), to financially support part of this work. A.M.-K. acknowledges discussions with Ming-Hao Liu and Jia-Tong Shi and acknowledges partial support by the program "Excellence Initiative—Research University" for the AGH University of Krakow and by the Polish High-Performance Computing Infrastructure PLGrid (HPC Center: ACK Cyfronet AGH) for providing computer facilities and support within computational grant no. PLG/2024/017407. K.W. and T.T. acknowledge support from the JSPS KAKENHI (grant nos. 21H05233 and 23H02052) and World Premier International Research Center Initiative (WPI), MEXT, Japan.

REFERENCES

(1) Settnes, M.; Power, S. R.; Brandbyge, M.; Jauho, A. P. Graphene Nanobubbles as Valley Filters and Beam Splitters. *Phys. Rev. Lett.* **2016**, *117*, 1−5.

(2) Shayeganfar, F. Strain Engineering of Electronic Properties and Anomalous Valley Hall Conductivity of Transition Metal Dichalcogenide Nanoribbons. *Sci. Rep* **2022**, *12*, 1−14.

(3) Milovanović, S. P.; Peeters, F. M. Strain Controlled Valley Filtering in Multi-Terminal Graphene Structures. *Appl. Phys. Lett.* **2016**, *109*, No. 203108.

(4) Šrut Rakić, I.; Gilbert, M. J.; Sarkar, P.; Aishwarya, A.; Polini, M.; Madhavan, V.; Mason, N. Interaction Effects and Non-Integer Pseudo-Landau Levels in Engineered Periodically Strained Graphene. *Nano Lett.* **2025**, *25*, 41−47.

(5) Shi, H.; Zhan, Z.; Qi, Z.; Huang, K.; Veen, E. V.; Silva-Guillén, J. Á.; Zhang, R.; Li, P.; Xie, K.; Ji, H.; Katsnelson, M. I.; Yuan, S.; Qin, S.; Zhang, Z. Large-Area, Periodic, and Tunable Intrinsic Pseudo-Magnetic Fields in Low-Angle Twisted Bilayer Graphene. *Nat. Commun.* **2020**, *11*, 371.

(6) Zhou, H.; Auerbach, N.; Uzan, M.; Zhou, Y.; Banu, N.; Zhi, W.; Huber, M. E.; Watanabe, K.; Taniguchi, T.; Myasoedov, Y.; Yan, B.; Zeldov, E. Imaging Quantum Oscillations and Millitesla Pseudomagnetic Fields in Graphene. *Nature* **2023**, *624*, 275−281.

(7) Levy, N.; Burke, S. A.; Meaker, K. L.; Panlasigui, M.; Zettl, A.; Guinea, F.; Neto, A. H. C.; Crommie, M. F. Strain-Induced Pseudo-Magnetic Fields Greater than 300 T in Graphene Nanobubbles. *Science* **2010**, *329*, 544−547.

(8) Milovanović, S. P.; Covaci, L.; Peeters, F. M. Strain Fields in Graphene Induced by Nanopillar Mesh. *J. Appl. Phys.* **2019**, *125*, No. 082534.

(9) Peng, Z.; Chen, X.; Fan, Y.; Srolovitz, D. J.; Lei, D. Strain Engineering of 2D Semiconductors and Graphene: From Strain Fields to Band-Structure Tuning and Photonic Applications. *Light: Science and Applications.* **2020**, *9*, 190.

(10) Zhu, S.; Huang, Y.; Klimov, N. N.; Newell, D. B.; Zhitenev, N. B.; Stroscio, J. A.; Solares, S. D.; Li, T. Pseudomagnetic Fields in a Locally Strained Graphene Drumhead. *Phys. Rev. B* **2014**, *90*, No. 075426.

(11) Solin, S. A.; Thio, T.; Hines, D. R.; Heremans, J. J. Enhanced Room-Temperature Geometric Magnetoresistance in Inhomogeneous Narrow-Gap Semiconductors. *Science* **2000**, *289*, 1530−1532.

(12) Lu, J.; Zhang, H.; Shi, W.; Wang, Z.; Zheng, Y.; Zhang, T.; Wang, N.; Tang, Z.; Sheng, P. Graphene Magnetoresistance Device in van Der Pauw Geometry. *Nano Lett.* **2011**, *11*, 2973−2977.

(13) Rowe, A. C. H.; Hines, D. R.; Solin, S. A. Enhanced Room-Temperature Piezoconductance of Metal-Semiconductor Hybrid Structures. *Appl. Phys. Lett.* **2003**, *83*, 1160−1162.

(14) Hewett, T. H.; Kusmartsev, F. V. Geometrically Enhanced Extraordinary Magnetoresistance in Semiconductor-Metal Hybrids. *Phys. Rev. B* **2010**, *82*, No. 212404.

(15) Sun, J.; Gooneratne, C. P.; Kosel, J. Design Study of a Bar-Type EMR Device. *IEEE Sens. J.* **2012**, *12*, 1356−1360.

(16) Sun, J.; Patil, S. B.; Soh, Y. A.; Kose, J. Strong Temperature Dependence of Extraordinary Magnetoresistance Correlated to Mobility in a Two-Contact Device. *Appl. Phys. Express* **2012**, *5*, No. 033002.

(17) Sun, J.; Soh, Y. A.; Kosel, J. Geometric Factors in the Magnetoresistance of N-Doped InAs Epilayers. *J. Appl. Phys.* **2013**, *114*, No. 203908.

(18) Friedman, A. L.; Robinson, J. T.; Perkins, F. K.; Campbell, P. M. Extraordinary Magnetoresistance in Shunted Chemical Vapor Deposition Grown Graphene Devices. *Appl. Phys. Lett.* **2011**, *99*, No. 022108.
(19) Möller, C. H.; Kronenwerth, O.; Grundler, D.; Hansen, W.; Heyn, C.; Heitmann, D. Extraordinary Magnetoresistance Effect in a Microstructured Metal-Semiconductor Hybrid Structure. *Appl. Phys. Lett.* **2002**, *80*, 3988−3990.
(20) Hewett, T. H.; Kusmartsev, F. V. Extraordinary Magnetoresistance: Sensing the Future. *Central European Journal of Physics* **2012**, *10*, 602−608.
(21) Zhou, B.; Watanabe, K.; Taniguchi, T.; Henriksen, E. A. Extraordinary Magnetoresistance in Encapsulated Monolayer Graphene Devices. *Appl. Phys. Lett.* **2020**, *116*, No. 053102.
(22) Zhou, B.; Watanabe, K.; Taniguchi, T. Extraordinary Magnetoresistance in High-Quality Graphene Devices with Daisy Chains and Fermi-Level Pinning. *Phys. Rev. Appl.* **2024**, *22*, No. 064046.
(23) Miao, X.; Tongay, S.; Hebard, A. F. Strain-Induced Suppression of Weak Localization in CVD-Grown Graphene. *J. Phys.: Condens. Matter* **2012**, *24*, No. 475304.
(24) Guinea, F.; Katsnelson, M. I.; Geim, A. K. Energy Gaps and a Zero-Field Quantum Hall Effect in Graphene by Strain Engineering. *Nat. Phys.* **2010**, *6*, 30−33.
(25) Masubuchi, S.; Iguchi, K.; Yamaguchi, T.; Onuki, M.; Arai, M.; Watanabe, K.; Taniguchi, T.; MacHida, T. Boundary Scattering in Ballistic Graphene. *Phys. Rev. Lett.* **2012**, *109*, No. 036601.
(26) Thornton, T. J.; Roukes, M. L.; Scherer, A.; Van De Gaag, B. P. Boundary Scattering in Quantum Wires. *Phys. Rev. Lett.* **1989**, *63*, 2128−2131.
(27) Tahir, M.; Schwingenschlögl, U. Beating of Magnetic Oscillations in a Graphene Device Probed by Quantum Capacitance. *Appl. Phys. Lett.* **2012**, *101*, No. 013114.
(28) Cui, L. J.; Zeng, Y. P.; Zhang, Y.; Zhou, W. Z.; Shang, L. Y.; Lin, T.; Chu, J. H. Beating Patterns in the Shubnikov-de Haas Oscillations Originated from Spin Splitting in In0.52Al0.48As/In0.65Ga0.35As Heterostructures: Experiment and Calculation. *Physica E Low Dimens Syst. Nanostruct* **2016**, *83*, 114−118.
(29) Konschuh, S.; Gmitra, M.; Fabian, J. Tight-Binding Theory of the Spin-Orbit Coupling in Graphene. *Phys. Rev. B* **2010**, *82*, No. 245412.
(30) Amann, J.; Völkl, T.; Rockinger, T.; Kochan, D.; Watanabe, K.; Taniguchi, T.; Fabian, J.; Weiss, D.; Eroms, J. Counterintuitive Gate Dependence of Weak Antilocalization in Bilayer Graphene/ WSe2 Heterostructures. *Phys. Rev. B* **2022**, *105*, No. 115425.
(31) Sun, L.; Rademaker, L.; Mauro, D.; Scarfato, A.; Pásztor, Á.; Gutiérrez-Lezama, I.; Wang, Z.; Martinez-Castro, J.; Morpurgo, A. F.; Renner, C. Determining Spin-Orbit Coupling in Graphene by Quasiparticle Interference Imaging. *Nat. Commun.* **2023**, *14*, 3771.
(32) Avsar, A.; Tan, J. Y.; Taychatanapat, T.; Balakrishnan, J.; Koon, G. K. W.; Yeo, Y.; Lahiri, J.; Carvalho, A.; Rodin, A. S.; O'Farrell, E. C. T.; Eda, G.; Castro Neto, A. H.; Özyilmaz, B. Spin-Orbit Proximity Effect in Graphene. *Nat. Commun.* **2014**, *5*, 4875.
(33) De Sanctis, A.; Mehew, J. D.; Alkhalifa, S.; Withers, F.; Craciun, M. F.; Russo, S. Strain-Engineering of Twist-Angle in Graphene/HBN Superlattice Devices. *Nano Lett.* **2018**, *18*, 7919−7926.
(34) Yang, B.; Tu, M. F.; Kim, J.; Wu, Y.; Wang, H.; Alicea, J.; Wu, R.; Bockrath, M.; Shi, J. Tunable Spin-Orbit Coupling and Symmetry-Protected Edge States in Graphene/WS2. *2d Mater.* **2016**, *3*, No. 031012.
(35) Couto, N. J. G.; Costanzo, D.; Engels, S.; Ki, D. K.; Watanabe, K.; Taniguchi, T.; Stampfer, C.; Guinea, F.; Morpurgo, A. F. Random Strain Fluctuations as Dominant Disorder Source for High-Quality on-Substrate Graphene Devices. *Phys. Rev. X* **2014**, *4*, No. 041019.
(36) Wang, L.; Makk, P.; Zihlmann, S.; Baumgartner, A.; Indolese, D. I.; Watanabe, K.; Taniguchi, T.; Schönenberger, C. Mobility Enhancement in Graphene by in Situ Reduction of Random Strain Fluctuations. *Phys. Rev. Lett.* **2020**, *124*, No. 157701.
(37) Tikhonenko, F. V.; Kozikov, A. A.; Savchenko, A. K.; Gorbachev, R. V. Transition between Electron Localization and Antilocalization in Graphene. *Phys. Rev. Lett.* **2009**, *103*, No. 226801.
(38) Laitinen, A.; Kumar, M.; Hakonen, P. J. Weak Antilocalization of Composite Fermions in Graphene. *Phys. Rev. B* **2018**, *97*, No. 075113.
(39) Gopinadhan, K.; Shin, Y. J.; Yudhistira, I.; Niu, J.; Yang, H. Giant Magnetoresistance in Single-Layer Graphene Flakes with a Gate-Voltage-Tunable Weak Antilocalization. *Phys. Rev. B* **2013**, *88*, No. 195429.
(40) Shioya, H.; Russo, S.; Yamamoto, M.; Craciun, M. F.; Tarucha, S. Electron States of Uniaxially Strained Graphene. *Nano Lett.* **2015**, *15*, 7943−7948.
(41) Khatibi, Z.; Rostami, H.; Asgari, R. Valley Polarized Transport in a Strained Graphene Based Corbino Disc. *Phys. Rev. B* **2013**, *88*, 1−9.
(42) Amasay, J.; Sela, E. Transport through Dynamic Pseudogauge Fields and Snake States in a Corbino Geometry. *Phys. Rev. B* **2021**, *104*, 1−10.
(43) Wang, L.; Meric, I.; Huang, P. Y.; Gao, Q.; Gao, Y.; Tran, H.; Taniguchi, T.; Watanabe, K.; Campos, L. M.; Muller, D. A.; Guo, J.; Kim, P.; Hone, J.; Shepard, K. L.; Dean, C. R. One-Dimensional Electrical Contact to a Two-Dimensional Material. *Science* **2013**, *342*, 614−617.
(44) Mann, S.; Kumar, R.; Jindal, V. K. Negative Thermal Expansion of Pure and Doped Graphene. *RSC Adv.* **2017**, *7*, 22378−22387.
(45) McQuade, G. A.; Plaut, A. S.; Usher, A.; Martin, J. The Thermal Expansion Coefficient of Monolayer, Bilayer, and Trilayer Graphene Derived from the Strain Induced by Cooling to Cryogenic Temperatures. *Appl. Phys. Lett.* **2021**, *118*, No. 203101.
(46) Edeskuty, F. J.; Stewart, W. F. *Safety in the Handling of Cryogenic Fluids*; Springer: New York, NY, 1996. .
(47) Barron, T. H. K.; Collins, J. G.; White, G. K. Thermal Expansion of Solids at Low Temperatures. *Adv. Phys.* **1980**, *29*, 609−730.
(48) Liu, M. H.; Rickhaus, P.; Makk, P.; Tóvári, E.; Maurand, R.; Tkatschenko, F.; Weiss, M.; Schönenberger, C.; Richter, K. Scalable Tight-Binding Model for Graphene. *Phys. Rev. Lett.* **2015**, *114*, 1−5.
(49) Mreńca-Kolasińska, A.; Chen, S. C.; Liu, M. H. Probing Miniband Structure and Hofstadter Butterfly in Gated Graphene Superlattices via Magnetotransport. *NPJ. 2D Mater. Appl.* **2023**, *7*, 1−9.
(50) Baranger, H. U.; Stone, A. D. Electrical Linear-Response Theory in an Arbitrary Magnetic Field: A New Fermi-Surface Formation. *Phys. Rev. B* **1989**, *40*, 8169−8193.
(51) Mreńca-Kolasińska, A.; De Beule, C.; Shi, J.-T.; Garcia-Ruiz, A.; Kochan, D.; Richter, K.; Liu, M.-H. Pseudomagnetotransport in Strained Graphene. *ArXiv* **2025**. .
(52) Kolasiński, K.; Szafran, B.; Brun, B.; Sellier, H. Interference Features in Scanning Gate Conductance Maps of Quantum Point Contacts with Disorder. *Phys. Rev. B* **2016**, *94*, 1−11.
(53) Datta, S. *Electronic Transport in Mesoscopic Systems*; Cambridge University Press: 1995. .
(54) Büttiker, M. Four-Terminal Phase-Coherent Conductance. *Phys. Rev. Lett.* **1986**, *57*, 1761−1764.

https://doi.org/10.1021/acsnano.5c04844
ACS Nano 2025, 19, 29276−29285